HIGH-RESOLUTION IMAGING OF DIFFRACTIONS - A STEERED MUSIC APPROACH

L.-J. Gelius, M. Tygel, A.K. Takahata, E.G. Asgedom, and D.R. Serrano

email: *mtygel@gmail.br*

keywords: *Signal processing, diffractions, MUSIC, migration*

ABSTRACT

Enhancement of diffractions and their use to increase the resolution of finer details in a seismic image has been a popular research topic the later years. It is well recognized that diffractions carry useful information about small scale characteristics associated with, e.g., faults, pinch-outs, wedge-outs and other geological features often linked to potential hydrocarbon reservoirs. To extract the information content of these diffractions and form an optimal image of local subsurface details is not a trivial task. The conventional way to image diffractions is using standard migration techniques, essentially based on wave propagation. However, limited acquisition aperture, as well as finite bandwidth of the seismic data, imposes on migration techniques a so-called diffraction-limit resolution constraint, by which the full use of the diffraction information available within the data is prevented. An alternative to overcome such limitations is to turn to signal-processing oriented approaches, which focus at the structural features of data (e.g., singular properties of covariance matrices), with the aim of detecting and imaging desired events. With an interest on diffractions, we propose here a windowed or steered version of the powerful signal-processing scheme, MUltiple SIgnal Classification (MUSIC) method. Use of this new scheme ensures that diffractions can be imaged to a resolution beyond the classical limit. The potential of this technique is demonstrated using both controlled and field data.

INTRODUCTION

The early use of seismic diffractions dates back to the pioneering works of Krey (1952), Haagedorn (1954) and Krey (1960). During the later years much attention has been paid to the enhancement and separation of diffractions from reflection data for a number of imaging purposes. Several approaches have been proposed, among them the use of anti-stationary filtering (Moser and Howard, 2008), plane-wave destruction filters (Fomel et al., 2007), Multi-focusing (MF) (Berkovitch et al., 2009) or Common Reflection Surface (CRS) (Asgedom et al., 2011, 2012b,a) moveout expressions. Since the diffracted events are known to carry high-resolution information about the subsurface, their optimal use in imaging is an important topic. In a recent paper (Gelius and Asgedom, 2011) discussed the concept of resolution from a theoretical point of view. Their analysis covered both the classical resolution limit (generally referred to as diffraction-limited imaging), as well as the use of high-coherency methods like MUltiple SIgnal Classification (MUSIC) (Schmidt, 1986). An attractive feature of the latter type of techniques is their potential to give rise to images with a resolving power beyond those of the classical limits (referred to as super-resolution images). The work accounted for here can be regarded as a practical demonstration of the conceptual ideas presented by Gelius and Asgedom (2011). Note, however, that in the referred paper time-reversal type of MUSIC was considered and not classical MUSIC as discussed here. More specifically, by means of illustrative examples, we verify that the use of a standard migration type of method will not be able to honor fully the potential high-resolution information carried by the diffractions. As a way to overcome such limitations, we propose to use a windowed or steered MUSIC type of algorithm to better preserve the finer details in the image. This technique has already been used by the authors with success in a series of publications related to diffraction

enhancement (Asgedom et al., 2011, 2012a). However, the details of the actual method have not been addressed. The main purpose of this paper is, thus, to introduce the basics of the proposed technique in a clear and concise manner. The actual performance of the method is also demonstrated employing two different data sets. This paper is organized as follows: After this introduction, a small section reviews the concepts of resolution and diffraction-limit. The next section introduces a simple numerical example to illustrate the resolution limitations of conventional imaging (e.g., backpropagation/migration), as a consequence of the so-called diffraction-limit condition, as generally attached to those methods. In the subsequent section, the same synthetic example is employed to show how the proposed version of the MUSIC algorithm leads to so-called super-resolution images, namely ones that overcome the classical diffraction-limit condition. The next section applies the new algorithm to a field data set and discusses its results. Finally, sections conclusions, acknowledgments and references complete the paper.

BASIC CONCEPT OF RESOLUTION AND A DIFFRACTION-LIMITED SYSTEM

According to Sheriff (1991) 'resolution is the ability to separate two features that are very close together; the minimum separation of two bodies before their individual properties are lost'. In case of a finite receiver array, it is well known that the directivity degrades causing a wider main lobe and increasing side lobes (Berkhout, 1984). This loss in resolution can be approximately described by the classical Rayleigh criterion:

$$\Delta l = \frac{L\lambda}{D} \,, \tag{1}$$

where l is the spatial resolution limit, D is the aperture or length of the array, L is the distance to the target and λ is the (dominant) wavelength. Such a system is denoted "diffraction limited". The same phenomenon can be analyzed from an imaging point of view by "backpropagating" scattered waves associated with point scatterers.

A SIMPLE NUMERICAL EXAMPLE

Consider the simple geometry shown in Fig.1 involving two nearby point scatterers, embedded in a homogeneous model and illuminated by a point source, and with the scattered data measured at receivers distributed over a surface S. For definiteness, we assume the vectors $\mathbf{r}_s = \mathbf{0}$ (origin), $\mathbf{r}_{sc}^k$ $(k = 1, 2)$, $\mathbf{r}$ and

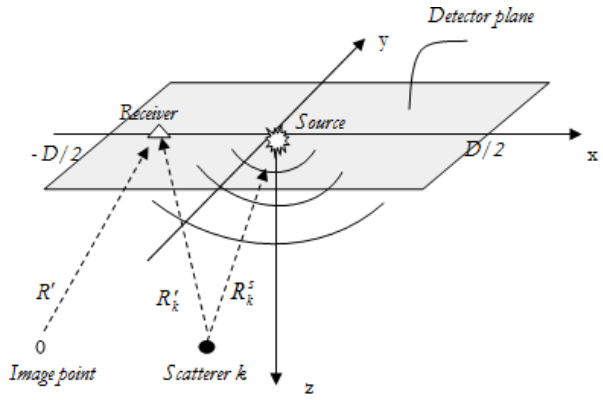

Figure 1: Sketch of scattering geometry.

$\mathbf{r}'$ to designate the source, scatterers, image and receiver points, respectively. Our analysis is carried out in the frequency domain, the frequency variable being denoted by ω. As a reasonable approximation, we assume that the scattered field, $p_{sc}(\mathbf{r}', \omega)$ observed at a receiver, has the form (Born type)

$$p_{sc}(\mathbf{r}', \omega) = \frac{\omega^2 s(\omega)}{c^2} \sum_{k=1}^{2} \frac{\exp[i\omega(\tau_k^s + \tau_k')]}{R_k^s R_k'} \,, \tag{2}$$

where c is the medium velocity, $R_k^s = |\mathbf{r}_{sc}^k|$ and $R_k' = |\mathbf{r}_{sc}^k - \mathbf{r}'|$ are the distances between the source and,

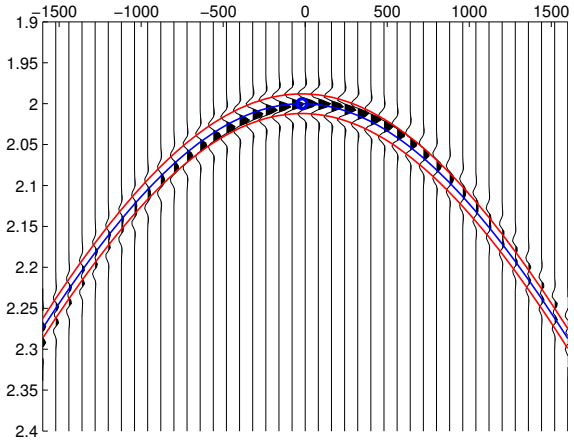

Figure 2: Seismic section of the two nearby diffractions.

respectively, the k-th scatterer and the receiver, with $\tau_k^s = R_k^s/c$ and $\tau_k' = R_k'/c$ being their corresponding traveltimes. Also, $s(\omega)$ represents the spectrum of the source pulse, for convenience chosen to be the zero-phase Ricker wavelet

$$s(\omega) = \frac{1}{\pi^{3/2}} \left(\frac{\omega^2}{\omega_0^3} \right) \exp[-\omega^2/\omega_0^2] \,, \tag{3}$$

where ω_0 represents the peak frequency. For computation simplicity, we assume that the measurement boundary is flat and characterized by an infinite aperture cross-line (y-direction) and a finite aperture (D) inline (x-direction). Moreover, we restrict the receivers to lie on a single horizontal (x-direction) line and that the source, scatterers and receiver line all lie on a single vertical z-plane. Such conditions define a so-called 2.5D configuration for which 3D wavefield computations on each receiver can be approximated by a single spatial (x-coordinate) integral (see, e.g., Bleistein, 1986). Under the above conditions, we have that $\mathbf{r}_{sc}^k = (x_{sc}^k, 0, z_{sc}^k)$, $\mathbf{r} = (x, 0, z)$ and $\mathbf{r}' = (x', 0, 0)$ $(-D < x' < D)$. As a consequence, we find

$$R_k' = \sqrt{(x' - x_{sc}^k)^2 + (z_{sc}^k)^2}, \quad R_k' = \sqrt{(x' - x)^2 + z^2}, \quad \tau_k' = R_k'/c \quad \text{and} \quad \tau' = R'/c \,. \tag{4}$$

In the simulations, we used a medium velocity c = 2000m/s, an aperture D = 3200m and an equal depth L = 2000m of the two nearby scatterers. Moreover, the center frequency was chosen as f_0 = 25Hz. This corresponds to a center wavelength ω_0 =80m. Replacing λ by λ_0 in Eq.(1) gives that the smallest distance that can be resolved according to the Rayleigh criterion is approximately $\Delta l \approx 5\lambda_0/8$. With the above configuration, we obtain the data set of Fig.2

IMAGING BY BACKPROPAGATION

We now use the conventional approach of backpropagation to image of data with the aim of retrieving the scatterer positions in depth. Following, e.g., Schneider (1978), Esmersoy and Oristaglio (1988), Schleicher et al. (2007), Gelius and Asgedom (2011), the backpropagated wavefield, $p_{bp}(\mathbf{r}', \omega)$, can be expressed by an integral of the form

$$p_{bp}(\mathbf{r}', \omega) = - \int\int_S \left[\frac{\partial}{\partial n} G_0^*(\mathbf{r}, \mathbf{r}', \omega) p_{sc}(\mathbf{r}', \omega) - G_0^*(\mathbf{r}, \mathbf{r}', \omega) \frac{\partial}{\partial n} p_{sc}(\mathbf{r}', \omega) \right] d\mathbf{r}' \,. \tag{5}$$

Following, e.g., Bleistein (1986), the above integral admits a stationary-phase, approximate evaluation of the cross-line (y-coordinate) integral, taken as an inner integral in Eq.(5), so that we are left with an integration over the inline, x-coordinate only. If we divide the backpropagated field by the source field

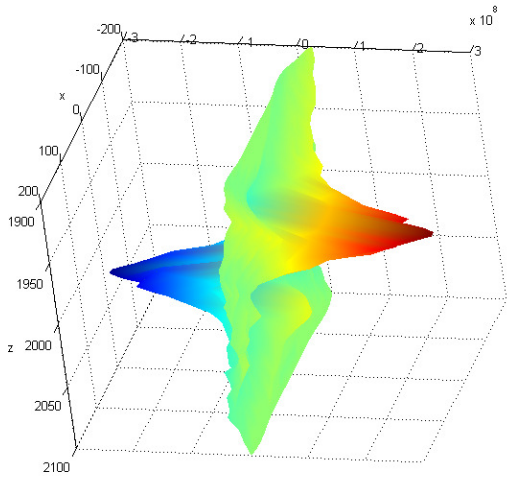

(a)

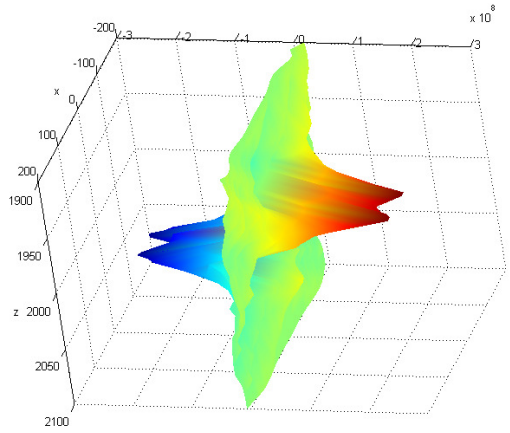

(b)

Figure 3: Migrated image of two nearby scatterer separated by (a) $5\lambda_0/8$ and (b) λ_0 (λ_0 being the center wavelength).

incident at each image point (i.e., we apply the U/D imaging condition), then summing over the available bandwidth will give the final migrated image $I(\mathbf{r}) = I(x, 0, z)$ in the vertical cross-section defined by $y = 0$:

$$I(\mathbf{r}) \approx \begin{cases} \sqrt{\dfrac{8\pi}{c}} \displaystyle\int_0^{\omega_B} \omega^{5/2}\, s(\omega) \int_{-D/2}^{D/2} \frac{(R' z_{sc} + R'_{sc} z)}{\sqrt{R' R'_{sc} |\Delta|}} \cos\left[\frac{\omega\Delta}{c} + \frac{\pi}{2}\left(1 - \frac{\mathrm{sgn}\Delta}{2}\right)\right] dx\, d\omega, & (\Delta \neq 0), \\ 0, \quad (\Delta = 0)\,, \end{cases} \tag{6}$$

where the notation $\Delta = R'_{sc} - R'$ has been used. Figure 3a shows the migrated image of the two scatterers when separated a distance of Δl (only a selected part of the image surrounding the two scatterers shown for convenience). It can easily be seen that migration is not able to resolve the two features. This example demonstrates that the Rayleigh criterion is an empirical measure only able to give an approximate estimate of the actual diffraction limit of a system. By increasing the scatterer separation to λ_0, it follows from Fig.3b that the two scatterers now separates well as expected. In the next section, we will discuss an

alternative approach to image scattering events. The basis of this technique is to combine the data in a local window steered by the migration operator with a high-resolution coherency measure denoted MUltiple SIgnal Classification (MUSIC) Schmidt (1986). This MUSIC type of migration has the potential of imaging scatterers beyond the classical diffraction limit just discussed.

SEMBLANCE APPROACH TO DIFFRACTION-STACKING AND THE STEERED DATA WINDOW

In standard diffraction-stacking (Kirchhoff) type of migration, data are summed along the migration operator as defined by a given velocity model. Introduce now a small data window centered at the migration operator curve as shown in Fig.4. The upper red curve defines the start of the data window and follows the operator curve (interpolated to nearest data sample). This curve defines the start sample of each trace and the window length defined in time samples defines the length of each subtrace selected. It is also to be noted the analogy between the above windowing process with one associated with semblance in velocity analysis, which uses the stacking operator (NMO) instead of the migration operator curve. Both these operators are velocity dependent. For reasons that will be clear below, it is advantageous that values corresponding

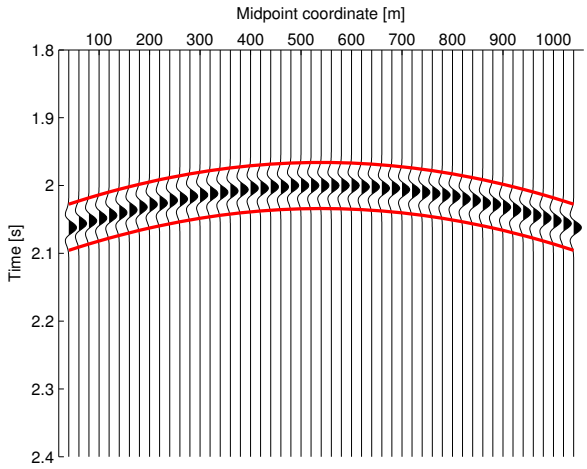

Figure 4: Window surrounding migration operator curve.

to the same sample number of each subtrace within the window are horizontally displayed as entries of a matrix line. One refers to that process as a steered matrix construction. The terminology is a reminder that the window steers the matrix. The benefit of the construction is that the window operations as required for the imaging methods become easily formulated as natural matrix operations. Another beneficial aspect is that approximation of trial curves to diffraction events within the window translates, after steering, into corresponding approximations to the horizontal, measurements of which being better suited to available signal-processing schemes. In particular, conventional semblance can be elegantly formulated in terms of the covariance of the steered matrix. The inner properties of that covariance matrix are, however, not made use of in the semblance calculation. That explains the trade-off of lower resolution and robustness that are characteristic of the semblance as a coherence measure. As well known, higher-resolution coherency measures, generally referred to as pseudo-spectra, can be achieved if the finer, eigenstructure properties of the covariance of the steered matrix are exploited, as is the case of the steered MUSIC considered here (see, e.g., Kirlin, 1992; Asgedom et al., 2011).

The concept of steered MUSIC has been previously employed by Kirlin (1992) to further improve the velocity analysis. However, as opposed to semblance, which produces normalized values between 0 and 1, MUSIC, despite its high-resolution capability, yields amplitudes (pseudo-spectra) of arbitrary values. Such unpleasant behavior makes the simple replacement of semblance with MUSIC as a coherency measure, for example in standard velocity analysis, not adequate. That is probably also the main reason why MUSIC

type of seismic signal analysis has not been much discussed the recent years. In order to condition the MUSIC pseudo-spectrum to be a normalized quantity, Asgedom et al. (2011) proposed semblance-balanced MUSIC. This idea will also be employed in the current work.

The above discussion and qualitative considerations of steered MUSIC already allows us, even without the technical details of the method, to appreciate its application to the numerical example earlier introduced. A particular motivation is the comparison with the counterpart results provided by conventional (backpropagation) obtained for the same example. That is what we do in the next section, leaving to the subsequent section the formal description of the steered MUSIC method.

APPLICATION OF STEERED MUSIC TO NUMERICAL EXAMPLE

Let us now revisit the scattering example from the previous section. Figure.5 shows the scattered data associated with the two nearby scatterers measured along the horizontal receiver line defined by y=0 (source-gather). The two red curves superimposed the same figure defines the data ('semblance') window computed around the true position of one of the scatterers. Figure 5b shows the corresponding steered data window. One can see near-horizontal events fairly well aligned (especially in the middle part of the window), but

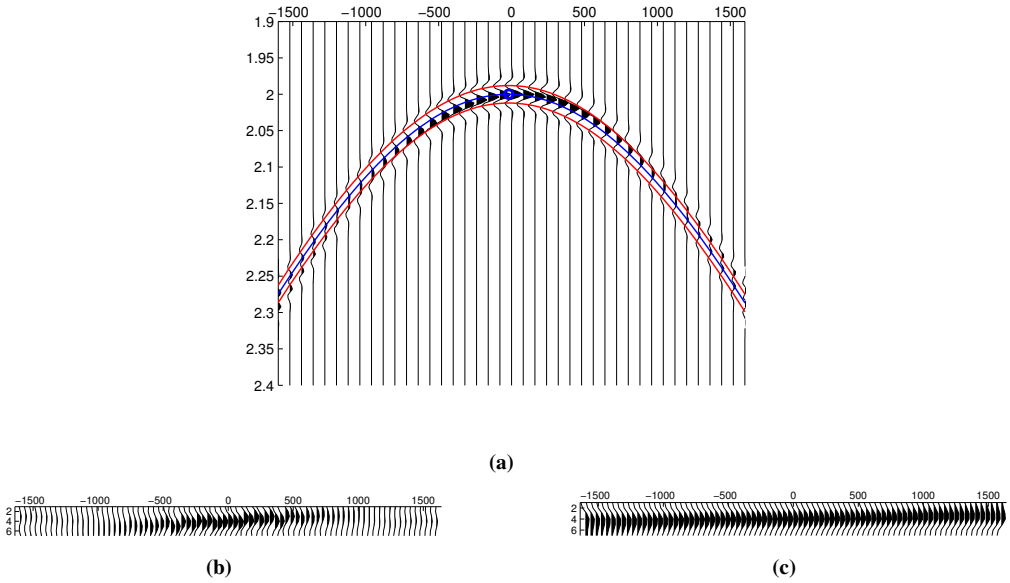

Figure 5: (a) Scattered data superimposed steered data window centered around one of the scatterers. (b) Raw steered data window. (c) After spatial smoothing and amplitude balancing.

with additional interfering events associated with the other nearby scatterer. The data within the window are therefore further processed by applying spatial smoothing (horizontal 2D filter) and amplitude balancing. The final result is shown in Fig.5c where the horizontal trend has been significantly enhanced. A fairly long data window has been used here for demonstration purposes. In practice, use of a shorter window can ensure a more robust result. The width of the data window has been chosen to seven time samples in this example. In general, the width should be chosen in a way that the main parts of the wavelet fall inside it. Figure 6 is similar to Fig.5, however with the difference that the data window is no longer centered around one of the scatterers but a nearby point. The steered data window now looks quite different both before and after further processing (Figs.6b-c), and no longer contains near-horizontally aligned events. We will now demonstrate the performance of steered MUSIC employing the scattered data set plotted in Figs.5a and 6a. The result is shown in Fig.7. We can easily see that the two nearby scatterers are well separated (only a selected part of the image surrounding the two scatterers shown for convenience). This result is certainly different from the migrated image shown in Fig.3a, demonstrating the high-resolution capability of the new proposed technique. Note that since MUSIC will only give the extreme localization of a scatterer, the effect of the pulse is no longer present (see Fig.7).

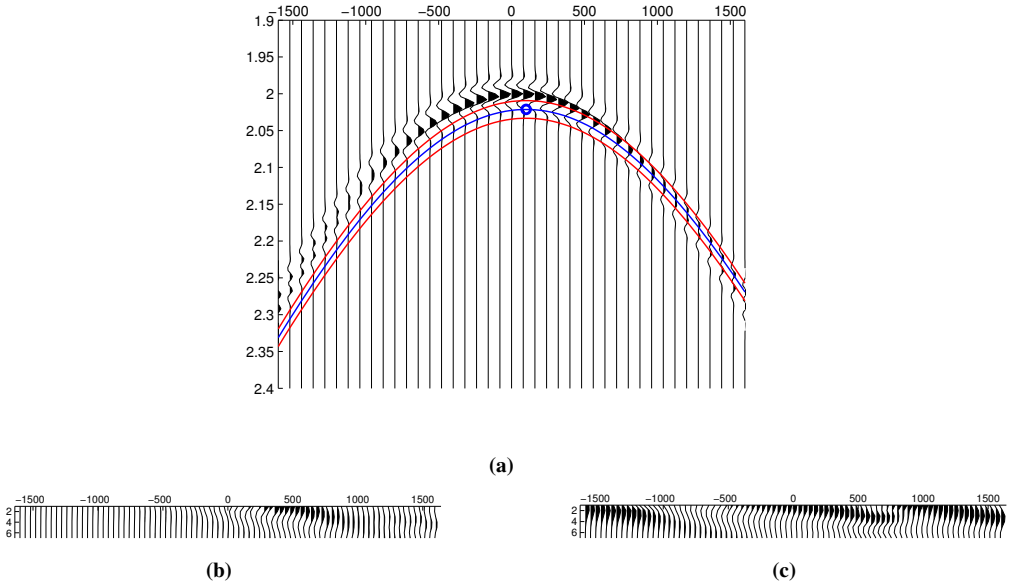

Figure 6: (a) Scattered data superimposed steered data window centered around a point nearby the two scatterers. (b) Raw steered data window. (c) After spatial smoothing and amplitude balancing.

DESCRIPTION OF STEERED MUSIC

Based on the simple simulations and observations made in the previous section, we consider the window steered data matrix, $\mathbf{D}$, that corresponds to a well-aligned scattering event (cf. Figs.5b-c). The matrix $\mathbf{D}$ can then be written in the form

$$\mathbf{D} = [\mathbf{m}_1, \mathbf{m}_2, \cdots, \mathbf{m}_{N_r}]^T \,, \tag{7}$$

where, $\mathbf{m}_i = [m_i(\Delta t), m_i(2\Delta t), \cdots, m_i(N_t \Delta t)]^T$, is a column vector representing the set of samples recorded by receiver i with $i = 1, 2 \cdots, N_r$ and Δt is the sample rate. Moreover, N_r and N_t denote the number of receivers and observed samples in each receiver, respectively. We now introduce the conceptual trace decomposition

$$\mathbf{m}_i = \mathbf{m}_{av} + \Delta\mathbf{m}_i + \mathbf{n}_i \,, \tag{8}$$

where

$$\mathbf{m}_{av} = \frac{1}{N_r} \sum_{i=1}^{N_r} \mathbf{m}_i \,, \tag{9}$$

is the average measurement vector associated with the window, Δm_i is the residual trace contribution and n_i is the noise. The above decomposition readily carries over to the steered data matrix $\mathbf{D}$, namely

$$\mathbf{D} = \mathbf{A} + \Delta\mathbf{A} + \mathbf{N} \,. \tag{10}$$

Here, all matrices have the dimension $N_r \times N_t$, where N_r is the number of traces within the window (aperture) and N_t is the number of time samples. Normally, $N_r > (>) N_t$. Moreover, we used the following definitions: $\mathbf{A} = [\mathbf{m}_{av}, \mathbf{m}_{av}, \cdots, \mathbf{m}_{av}]^T = \mathbf{u} \cdot \mathbf{m}_{av}^T$ with $\mathbf{u}$ the vector of ones, $\mathbf{u} = [1, 1, \cdots, 1]^T$, $\Delta\mathbf{A} = [\Delta\mathbf{m}_1, \Delta\mathbf{m}_2, \cdots, \Delta\mathbf{m}_{N_r}]^T$ and $\mathbf{N} = [\mathbf{n}_1, \mathbf{n}_2, \cdots, \mathbf{n}_{N_r}]^T$. A pictorial description of the matrix decomposition of Eq.(10) is provided by Fig.8. In terms of the decomposition of Eq. (10), the sample correlation matrix $\mathbf{R}$ (covariance matrix) of the steered matrix, $\mathbf{D}$, can be computed as

$$\mathbf{D} = \frac{1}{N_r}\mathbf{D}\mathbf{D}^T = \frac{1}{N_r}(\mathbf{A} + \Delta\mathbf{A} + \mathbf{N})(\mathbf{A} + \Delta\mathbf{A} + \mathbf{N})^T \approx (\mathbf{A}\mathbf{A}^T + \Delta\mathbf{A}\Delta\mathbf{A}^T + \mathbf{N}\mathbf{N}^T) \,. \tag{11}$$

It is assumed that the energy of the traces are well balanced and that the same therefore can be expected for the residual traces (because of incoherency between the three components assumed). As a last assumption, we consider that the residual traces are uncorrelated. Finally, assume that noise is a Gaussian white

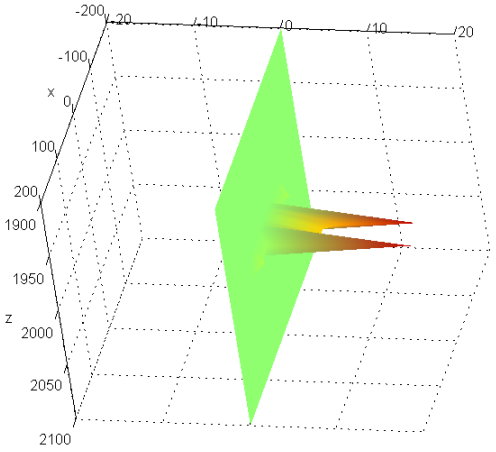

Figure 7: MUSIC migration of the two nearby scatterers.

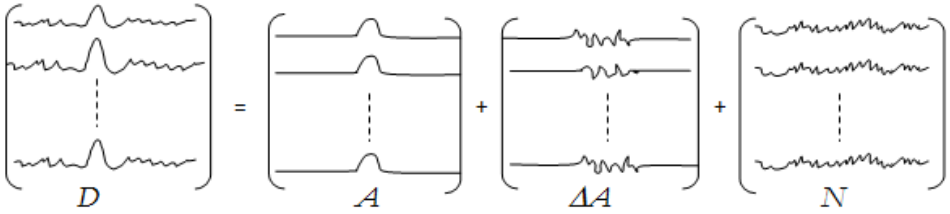

Figure 8: Decomposition of steered data matrix $(\mathbf{D})$, into three parts: average trace contribution $(\mathbf{A})$, residual trace $(\Delta\mathbf{A})$ and noise $(\mathbf{N})$ contributions.

realization. As a consequence, and assuming a migration operator defined by an optimal velocity field, the correlation matrix of Eq.(11) can be further approximated as

$$\mathbf{R} = \frac{||\mathbf{m}_{av}||^2}{N_t}\,\mathbf{u}\mathbf{u}^T + \frac{\varepsilon}{N_t}\,\mathbf{I} + \sigma_n^2\mathbf{I}\,, \tag{12}$$

in which the factor ε represents the energy of each residual trace and σ_n^2 is the variance of the white noise series. It is now straightforward to demonstrate that the vector $\mathbf{v} = \mathbf{u}/\sqrt{N_r}$ is an eigenvector of the correlation matrix $\mathbf{R}$. In fact,

$$\mathbf{R}\mathbf{v} = \frac{||\mathbf{m}_{av}||^2}{\sqrt{N_r}N_t}\,\mathbf{u}\mathbf{u}^T\mathbf{u} + \left(\frac{\varepsilon}{N_t} + \sigma_n^2\right)\mathbf{I}\frac{1}{\sqrt{N_r}}\,\mathbf{u} = \left[\frac{N_r||\mathbf{m}_{av}||^2}{N_t}\,\mathbf{u} + \frac{\varepsilon}{N_t} + \sigma_n^2\right]\mathbf{v} = \lambda\mathbf{v}\,, \tag{13}$$

with λ being the corresponding eigenvalue.

MUSIC is a sparsity technique that requires a larger number of observations than features to be resolved. If this requirement is fulfilled, the correlation matrix can be decomposed in two orthogonal spaces (respectively signal and nil spaces). In the case of steered MUSIC as discussed here, we have N_r multiple measurements of the same single horizontal event. Thus the fundamental requirement is well satisfied. Note also that, since the steering vector required to generate the MUSIC pseudo-spectrum is horizontal (cf. Eq.(13)), this implies that it is also frequency independent. This allows us to handle wideband seismic data Kirlin (1992).

The SVD of the correlation matrix R when computed from the actual data window can now be written formally as:

$$\mathbf{R} = \mathbf{V}_s\mathbf{\Sigma}_s\mathbf{V}_s^T + \mathbf{V}_n\mathbf{\Sigma}_n\mathbf{V}_n^T\,, \tag{14}$$

where $\mathbf{V}_s$ and $\mathbf{V}_n$ are, respectively, the signal and noise subspace singular-vector matrices, while $\mathbf{\Sigma}_s$ and $\mathbf{\Sigma}_n$ are the corresponding singular-value matrices.

We are now ready to define the MUSIC pseudo-spectrum at a given time sample, t_0 and mid-point coordinate, m_0. That is given by

$$I(m_0, t_0) = \frac{\mathbf{u}\mathbf{u}^T}{\mathbf{u}\mathbf{P}_n\mathbf{u}^T} \cdot w_{sb} \ , \tag{15}$$

where $\mathbf{P}_n = \mathbf{V}_n\mathbf{V}_n^T$ represents the (steered) noise subspace projection matrix and w_{sb} is the semblance-balancing factor healing the amplitude ambiguity of the classical MUSIC pseudo-spectrum (Asgedom et al., 2011). Note that, in case of a high-resolved localization event (such as a diffraction), the steering vector $\mathbf{u}$ has a negligible projection into the nil space and the pseudo-spectrum of Eq. (15) is expected to yield a large value.

The pseudo-spectrum in Eq.(15) is expressed by a nil-space projection. Alternatively, that pseudo-spectrum can be constructed employing its counterpart signal-space projection (Asgedom et al., 2012c). In the situation of more than one wavefront inside the data window, if a good velocity model is provided, one event will be well aligned and the other(s) will be slightly incoherent. As discussed above, the coherency can be further enhanced by simple sub-averaging or spatial smoothing. One may therefore assume that the dimension of the signal subspace of $\mathbf{R}$ is still one, and that only the largest eigenvector of the correlation matrix will span the signal subspace. However, in this work we have chosen to use the pseudo-spectrum in Eq.(15), which we believe is slightly more robust than its signal subspace counterpart (although more computer intensive).

DATA EXAMPLES

The potential of the proposed imaging technique will be now further demonstrated employing two different data sets. The first set is taken from the Marmousi model and represents a controlled test case. The second set is part of a marine seismic line acquired offshore Brazil including a well- known fault system.

4.1 **Marmousi model:** The Marmousi data set was generated by Institute Français du Petrol (IFP) employing a 2D finite-difference modeling code. It is based on a seismic profile running through the North Quenguela trough in the Cuanza basin in Angola. In this study, we selected the upper part of the original model containing a series of faults as shown in Fig.9a. Diffractions were enhanced employing the generalized Common-Reflection-Surface (CRS) technique. For more details about this enhancement as well as the Marmousi data the reader is referred to Asgedom et al. (2012a). The final zero-offset (ZO) diffraction-enhanced stack was then imaged using the steered MUSIC migration approach (cf. Fig.9b). The image is seen to be of high-resolution power with an overall good description of the major fault system including internal weaker faults. Since the synthetic data were generated employing the finite-difference technique, the model will slightly suffer from discretization artifacts. Thus a dipping reflector will be represented by a jig-saw pattern. Due to the high-resolution characteristics of MUSIC migration also these fine details are revealed (see right part of Fig.9b).

4.2 **Field data:** A 2D data set acquired over the Jequitinhonha basin (offshore Brazil) (Costa, 2011) was used to test the proposed imaging scheme. The basin has undergone extensional type of deformation. A very large extensional listric fault formed at the landward edge of the salt basin (Davison, 2007) divides it in two parts characterized by respectively shallow and deep water. Compressional deformations present in the basin are due to the salt. Figure 10 shows the seismic line (line 214-2660) selected for this study (post-stack migrated). It was acquired along a NE direction over the deep water part of the basin. The rectangle superimposed the migrated line defines the target zone which will be in focus here. This area includes a system of major and minor faults which are known to exist from this post-stack migrated reflection data, although not fully resolved.

Figure 11a shows a zoom of the target area defined in Fig.10 including an interpretation of the fault system. A diffraction-enhanced stack was computed for this same region based again on the generalized CRS technique. Note that this stack corresponded to a common-offset section with a very small offset of 150m. This diffraction stack was then migrated using both conventional Kirchhoff

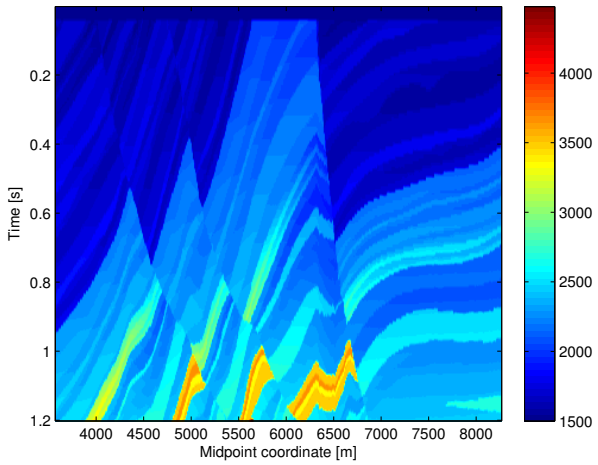

(a)

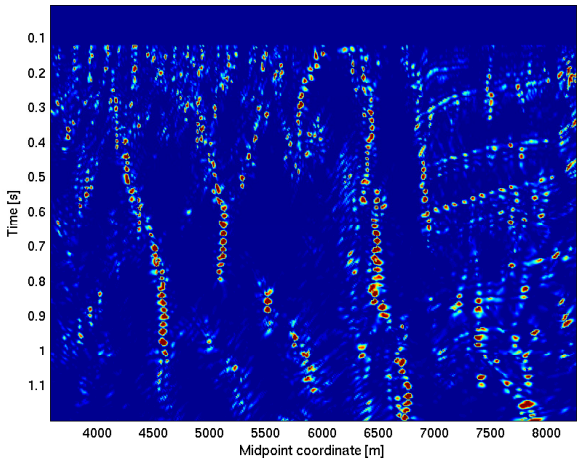

(b)

Figure 9: (a) Upper part of Marmousi velocity model and (b) MUSIC imaging of enhanced diffractions.

migration and MUSIC migration as advocated for in this paper (cf. Figs. 11b and c). The new high-resolution imaging technique is seen to give a more detailed picture than standard migration as expected. Also on comparison with the post-stack migrated image in Fig.11a, MUSIC migration is seen to give information which is highly correlated with the independent interpretation. In addition, MUSIC migration indicates another fault (encircled with red) which is not clearly visible on the post-stack migrated section.

DISCUSSION AND CONCLUSION

This paper has addressed the question of how to form a high-resolution image of diffracted wave contributions in seismic reflection data. Such diffractions can be observed in the seismic data set, as well as extracted by means of a diffraction-enhancement technique. Straightforward use of migration type of reconstruction methods will not be able to preserve the fully resolving power of diffractions, due to the diffraction-limit conditions inherently attached to those approaches. To be able to resolve finer details beyond the classical limits, we propose a new high-resolution imaging technique based on a windowed or

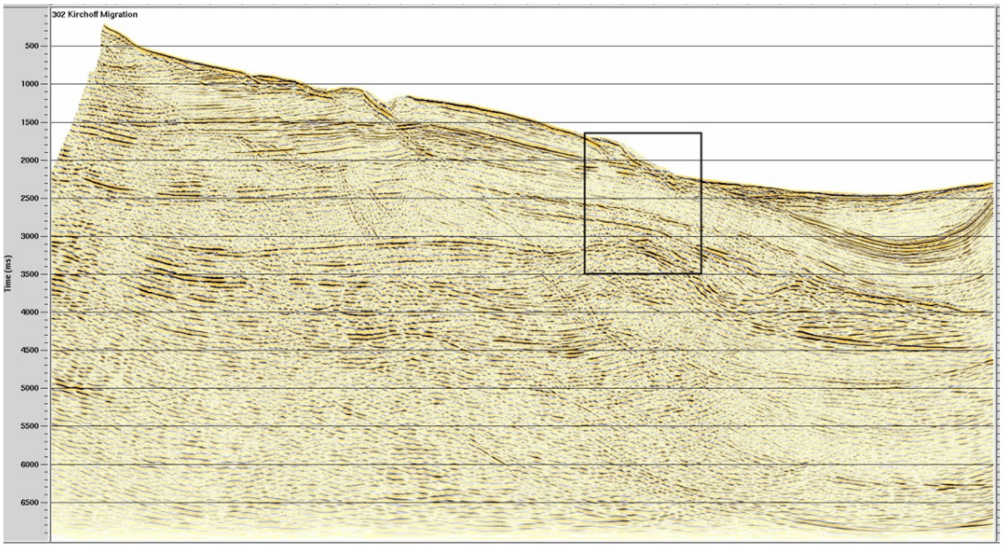

Figure 10: Seismic line 214-2660 superimposed target zone (post-stack migrated data).

steered MUSIC implementation. Application of the method on both synthetic and field data demonstrated a resolving power beyond that of standard migration. Note that the concept of MUSIC migration applies to all type of data sorting, time and depth domain as well as prestack and poststack. The only requirement is that data can be steered along the migration operator defined by an optimal velocity field.

ACKNOWLEDGEMENTS

The following institutions are acknowledged for support: A.K. Takahata, D. Rueda Serrano and M. Tygel: Petrobras - SCTC/Cepetro; L.-J. Gelius: Science Foundation of the State of São Paulo (FAPESP/Brazil), M. Tygel: National Council for Scientific and Technologic Development (CNPq/Brazil) and A.K. Takahata: Coordenação de Aperfeiçoamento de Pessoal de Nível Superior (CAPES/Brazil). We finally thank the WIT sponsors for kind support.

REFERENCES

Asgedom, E. G., Gelius, L.-J., and Tygel, M. (2011). Higher-resolution determination of zero-offset common-reflection-surface stack parameters. *International Journal of Geophysics, doi:10.1155/2011/819831*.

Asgedom, E. G., Gelius, L.-J., and Tygel, M. (2012a). 2-D pre- and post-stack diffraction separation and imaging. *Extended Abstract, 82nd Annual Meeting, Society of Exploration Geophysicists, Las Vegas, USA*.

Asgedom, E. G., Gelius, L.-J., and Tygel, M. (2012b). Seismic coherency measures in case of interfering events. *IEEE Signal Procsessing Magazine*, 47:47–56.

Asgedom, E. G., Gelius, L.-J., and Tygel, M. (2012c). Time-reversal multiple signal classification in case of noise: A phase-coherent approach. *J. Acoust. Soc. Am.*, 130:2024–2034.

Berkhout, A. J. (1984). Seismic resolution: a quantitative analysis of resolving power of acoustical echo techniques. *Geophysical Press*.

Berkovitch, A., Belfer, I., Hassin, Y., and Landa, E. (2009). Diffraction imaging by multifocusing. *Geophysics*, 74(6):WCA75–WCA81.

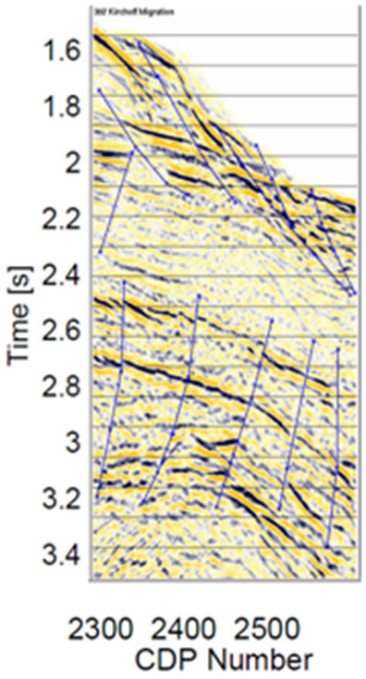

(a)

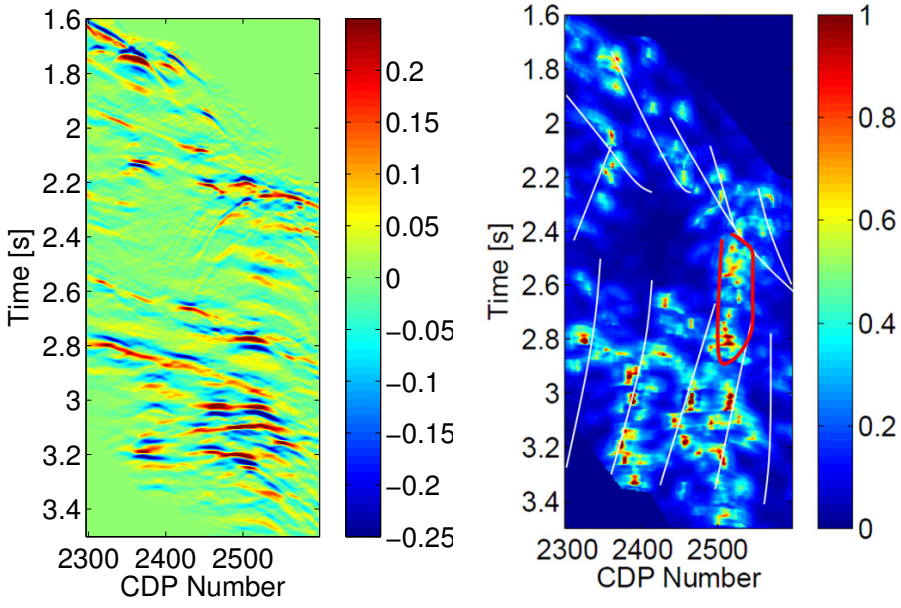

(b) (c)

Figure 11: (a) Target zone (post-stack migrated) with interpretation. (b) Standard Kirchhoff migration of enhanced diffractions. (c) MUSIC migration of the same diffracted events.

Bleistein, N. (1986). Two-and-one half dimensional in-plane wave propagation. *Geophys. Prosp.*, 34:686–703.

Esmersoy, C. and Oristaglio, M. (1988). Reverse-time wave-field extrapolation, imaging, and inversion. *Geophysics*, 52:920–931.

Fomel, S., Landa, E., and Taner, M. (2007). Poststack velocity analysis by separation and imaging of seismic diffractions. *Geophysics*, 72:89–94.

Gelius, L. .-J. and Asgedom, A. G. (2011). Diffraction-limited imaging and beyond - the concept of super resolution. *Geophys. Prosp.*, 59:400–421.

Haagedorn, J. G. (1954). A process of seismic reflection interpretation. *Geophys. Prosp.*, 2:85–127.

Kirlin, R. L. (1992). The relationship between semblance and eigenstructure velocity estimators. *Geophysics*, 57:1027–1033.

Krey, B. F. J. (1960). Diffraction problems in fault interpretation. *Geophys. Prosp.*, 8:381–388.

Krey, T. (1952). The significance of diffraction in the investigation of faults. *Geophysics*, 17:843–858.

Schleicher, J., Tygel, M., and Hubral, P. (2007). Seismic true-amplitude imaging. *Seismic Development Series,* SEG. 354 p.

Schmidt, R. O. (1986). Multiple emitter location and signal parameter estimation. *IEEE Trans. Antennas and Propagation*, AP-34:276–280.

Schneider, W. A. (1978). Integral formulation for migration in two and three dimensions. *Geophysics*, 43:49–76.